



CHORUS

This is the accepted manuscript made available via CHORUS. The article has been published as:

High-throughput ZT predictions of nanoporous bulk materials as next-generation thermoelectric materials: A material genome approach

Qing Hao, Dongchao Xu, Na Lu, and Hongbo Zhao

Phys. Rev. B **93**, 205206 — Published 31 May 2016

DOI: [10.1103/PhysRevB.93.205206](https://doi.org/10.1103/PhysRevB.93.205206)

High-throughput ZT predictions of nanoporous bulk materials as next-generation thermoelectric materials—a Material Genome approach

Qing Hao,^{1,*} Dongchao Xu,¹ Na Lu,² and Hongbo Zhao^{1,3,†}

¹*Department of Aerospace and Mechanical Engineering,
University of Arizona, Tucson, AZ 85721, USA*

²*Lyles School of Civil Engineering, Purdue University, West Lafayette, IN 47907, USA*

³*Laboratory of Quantum Engineering and Quantum Materials,
School of Physics and Telecommunication Engineering,
South China Normal University, Guangzhou, Guangdong 510006, China*

(Dated: April 25, 2016)

Abstract

The advancement of computational tools for material property predictions enables broad search of novel materials for various energy-related applications. However, challenges still exist in accurately predicting the mean free paths of electrons and phonons in a high throughput frame for thermoelectric property predictions, which largely hinders the computation-driven material search for novel materials. In this work, this need is eliminated under the limit of reduced nanostructure size within a bulk material, in which these mean free paths are restricted by the nanostructure size. A new criterion for ZT evaluation is proposed for general nanoporous bulk materials and is demonstrated with representative oxides.

PACS numbers: 84.60.Rb, 72.80.Tm, 66.70.Df

I. INTRODUCTION

Solid-state thermoelectric (TE) devices have the ability to directly convert heat into electricity for power generation.¹ Despite its many energy-harvesting applications, the potential impact of TE technology is largely hindered by the relatively low performance of commercial materials. In physics, the effectiveness of TE materials is evaluated by their TE figure of merit (ZT), defined as $ZT = S^2\sigma T/k$, where S , σ , k , and T represent Seebeck coefficient, electrical conductivity, thermal conductivity, and absolute temperature, respectively. Here k can be further split into lattice contribution k_L and electronic contribution k_E . Within the same material, challenge exists in obtaining a low k but a high power factor (PF) $S^2\sigma$. As the result, ZT s of commercial materials are still around unity after decades of research though $ZT > 2$ is preferred for TE to compete with other technologies. Along this line, nanostructured bulk materials, which are synthesized by hot pressing nanopowder into a bulk material, have been widely studied as an effective approach to improve ZT s of existing or novel materials.²⁻¹⁰ By introducing nanostructured interfaces or boundaries within a bulk material, the interdependent electron and phonon transport can be decoupled to dramatically reduce k_L but still maintain $S^2\sigma$, resulting in enhanced ZT . Unrestricted to conventional materials, this approach may also lead to high ZT s in unconventional TE materials with both a high $S^2\sigma$ and a high k_L , such as bulk Si.^{5,6} This will reach beyond conventional materials that heavily depend on toxic, rare, and expensive elements, e.g., Te used in Bi_2Te_3 and PbTe . In addition, the state-of-the-art TE materials are mostly restricted to sub-1000 K due to their low melting points, poor thermal stability, and/or serious oxidation over 1000 K. This restricts high-temperature (> 1000 K) TE power generation with much higher Carnot efficiency and thus more effective energy conversion though such heat sources are available in industrial applications. Beyond conventional SiGe alloys, promising TE materials for high temperatures have been identified in zintl-based compounds¹¹ and LaTe_y .¹²⁻¹⁴ However, these materials still involve rare elements such as La and Yb. With particular attention to high-temperature applications, broad material search is in urgent need for novel TE materials using nontoxic, cheap, and abundant elements. Such material discovery can be largely accelerated by the Materials Genome approach that uses first-principles computation to predict the TE properties of a new material.¹⁵⁻²⁰

For computation-driven TE material search, challenge still exists in accurately predicting the energy-dependent electron mean free path (MFP) l_E and phonon MFP l_P for TE property predictions. For phonon transport, there exist first-principles-based studies for standard materials such

as Si,²¹⁻²³ Ge,^{22,23} GaN,²⁴ BAs,²⁵ and PbTe.²⁶ However, such calculations are intrinsically very time-consuming and are limited to relatively simple material structures. In heavily doped TE materials, the strong point-defect scattering and electron scattering of phonons will add more uncertainties to the modeling. On the other hand, charge carriers are also affected by various scattering mechanisms, including acoustic/optical deformation potential scattering, ionized/neutral impurity scattering, non-polar/polar optical phonon scattering, and piezoelectric scattering.²⁷ In this situation, accurate electron modeling requires identifying scattering mechanisms for a given material and fitting the experimental data to determine parameters used in the model of each scattering mechanism. Without fitting parameters, first-principles methods have been developed to predict the scattering rates of charge carriers in Si,²⁸ Si_{1-x}Ge_x alloys,²⁹ GaAs and GaP.³⁰ These scattering rates can be further combined with the Boltzmann Transport Equation for the electrical property predictions.³¹ Similar to phonon studies, such first-principles electrical property predictions are still restricted to well-studied materials and are thus unsuitable for high-throughput material search, in which thousands of complicated materials will be screened based on the computed ZT s. As the result, high-throughput TE material search is mostly based on $S^2\sigma/\tau$ or the ZT s further estimated with guessed k_L/τ values,¹⁷⁻²⁰ where τ is the averaged relaxation time of all charge carriers. Similar simplification is also used for first-principles ZT estimation of standard TE materials.³²⁻³⁴ For materials screening, experimental inputs of σ and k_L are often required and the guidance from computations becomes very limited.

For nanostructured bulk materials, however, the need of computing electron and phonon MFPs can be eliminated when these MFPs are largely restricted by the nanostructure size, such as nanograin size or distance between nano-inclusions. In such materials, the optimum nanostructure size a should satisfy $l_E < a < l_P$ to reduce k_L without deteriorating σ . The maximum ZT is anticipated when a is reduced to l_E for majority charge carriers, called the small-grain-size limit for nanograined bulk materials.³⁵ With further decreased a , both the electrical and thermal conductivities will be scaled down with a as classical size effects, but S will remain the same with unchanged carrier concentration, resulting in saturated ZT . This simple treatment has been used to compare the power factor $S^2\sigma$ of new TE materials.^{15,16} However, the overall ZT is not evaluated without calculating k_L . In this work, we propose a ZT formulation of general materials under the limit of small nanostructures, which is solely based on phonon dispersions and electronic band structures predicted by first-principles calculations. For high-temperature applications, nanopores are employed to replace nanograins because ultra-fine nanograins are thermally unstable and will

grow up during long-term operations. In this case, the characteristic length a for pore-edge scattering of phonons and electrons is reduced to restrict the MFPs of heat and charge carriers for ZT enhancement. Unrestricted to nanograined or nanoporous bulk materials, such a peak ZT value can be called the small-nanostructure-size (SNS) limit without losing the generality. In calibrations with nanoporous bulk Si, this SNS estimation yields ZT close to the prediction by accurate models, which enables high-throughput material search for novel TE materials.

II. ZT ESTIMATION UNDER THE SNS LIMIT

A. Model description

In the SNS limit, electron and phonon MFPs are both limited by the nanostructure size a , i.e., $l_E = l_P = a$. For nanoporous bulk materials, a is the characteristic length related to the collision between pores and heat or charge carriers. Assuming diffusive phonon and electron scattering by pore edges, a is only dependent on the geometry of the porous structure,³⁶ i.e., the structure period and pore diameter. For largely separated nanopores, a can be estimated as $a = 2d/3\phi$, where d is diameter of nanopores and ϕ is porosity.³⁷ For samples with a high porosity, a becomes comparable to the spacing between adjacent nanopores. In this case, electrons and phonons will travel along the narrow neck between nanopores, which can be compared to phonon and electron transport along a nanowire.

With phonon and electron MFPs largely restricted by a , all quantities involved in ZT can be calculated. The electronic properties (S , σ , and k_E) can be calculated following standard procedures,^{20,38} which are described in Appendix A.

Given phonon dispersion $\omega_{i,\mathbf{q}}$ for state with branch index i and momentum \mathbf{q} , phonon group velocity $\mathbf{v}_{i,\mathbf{q}}^P$ can be calculated and lifetime can also be written as $\tau_{i,\mathbf{q}}^P = a/|\mathbf{v}_{i,\mathbf{q}}^P|$. Averaged over all three system directions, the lattice thermal conductivity k_L is given by the kinetic relationship as

$$k_L = \frac{1}{N\Omega} \sum_{i,\mathbf{q}} C(\omega_{i,\mathbf{q}}) a |\mathbf{v}_{i,\mathbf{q}}^P| / 3, \quad (1)$$

where N is total number of \mathbf{q} in the first Brillouin zone, Ω is volume of unit cell, and C is the contribution of phonon modes to the specific heat as given by

$$C(\omega) = k_B \left(\frac{\hbar\omega}{k_B T} \right)^2 \frac{\exp(\hbar\omega/k_B T)}{[\exp(\hbar\omega/k_B T) - 1]^2}. \quad (2)$$

In principle, the Eucken factor $(1 - \varphi)/(1 + \frac{\varphi}{2})$ should be multiplied to Eq. (1) to account for the reduced cross section area of heat transfer in a porous structure with porosity φ .^{39,40} The same factor should also be multiplied to σ and k_E , so that it will eventually cancel out in the ZT definition. Since φ is not specified in the calculations, the Eucken factor is not applied in the computed electrical and thermal conductivities but the computed ZT is unaffected. The predicted k_L , k_E , and σ can thus be viewed as those for a solid material with the same size effects for electrons and phonons. Dividing σ , k_E , and k_L with the common factor a , ZT of a material under the SNS limit can be computed as

$$ZT = \frac{S^2 \sigma T / a}{k_E / a + k_L / a}, \quad (3)$$

which can be further optimized at a given temperature by tuning the Fermi level E_F .

The employed electrical property calculations are carried out by modifying the package BOLTZTRAP,²⁰ where a constant electron MFP is assumed for charge carriers instead of a constant relaxation time in the original code. The full-band k_L calculation is similar to the electrical property calculations. Assigning a unity phonon group velocity in Eq. (1), the phonon code is calibrated with specific heat computations of bulk Si and ZnO, both of which agree within 2% with the experimental data from 50 to 300 K. The electronic band structures are given by the Vienna Ab-initio Simulation Package^{41,42} (VASP) based on the density functional theory using GGA approximation.⁴³ The phonon dispersions are calculated using PHONOPY package.⁴⁴

B. Calibration with nanoporous bulk silicon for its SNS limit

To evaluate the inaccuracy introduced by the SNS approximation, calibrations have been carried out on n-type nanoporous bulk Si using energy-dependent electron and phonon MFPs given for bulk Si.^{45,46} An electron concentration of $2 \times 10^{20} \text{ cm}^{-3}$ is used in the calculations. Only longitudinal acoustic (LA) and transverse acoustic (TA) phonons are considered for k_L calculations because no detailed expression of optical phonon MFPs is given in previous publications. In thermal conductivity calculations for phonons (Eq. (1)) and electrons, the characteristic length a is now replaced by the effective MFP l_{eff} modified from the bulk value l_{Bulk} , given as $l_{\text{eff}} = (l_{\text{Bulk}}^{-1} + a^{-1})^{-1}$. All employed parameters and detailed methods are given in Appendices B and C, respectively for electron and phonon calculations in this calibration.

Figure 1 shows the a -dependent $S^2 \sigma$, k_E , k_L , and ZT for nanoporous Si at 300 K and 1000 K.

Below 10 nm, ZT would saturate around the value for the SNS limit (~ 0.061 at 300 K and ~ 0.64 at 1000 K). The SNS limit k_E/a is higher at 1000 K due to thermally activated charge carriers. Due to the reduced phonon MFPs at elevated temperatures, the SNS limit requires much smaller structure size at 1000 K ($a < 3$ nm) than that for 300 K ($a \sim 10$ nm). In general, ZT s for the SNS limit (when $a \rightarrow 0$) and at $a = 10$ nm are comparable (5% divergence at 300 K, 38% at 1000 K). Therefore, the SNS limit can be used to estimate ZT s at $a \sim 10$ nm when l_E and l_P are unavailable. At ~ 10 nm structure size, the bulk electronic band structure is still valid (e.g., Si nanowires⁴⁷). However, measured k_L of real nanoporous Si films^{48–54} can often be much lower than predictions assuming bulk phonon transport and diffusive pore-edge phonon scattering. The SNS limit can thus be viewed as the lower ZT bound for nanoporous structures with 10 nm feature sizes.

FIG. 1. Nanostructure-size dependence of the calculated thermoelectric properties: (a) power factor $S^2\sigma$, (b) electronic thermal conductivity k_E , (c) lattice thermal conductivity k_L , and (d) ZT , of bulk Si using parabolic double-band model. Red circles and black squares are results at 300 K and 1000 K, respectively.

Despite different parameters used in the analysis, the trend of temperature-dependent TE properties is consistent with previous analysis for nanograined bulk Si that has improved ZT due to k_L reduction by grain-boundary phonon scattering.⁶ In real samples, charge carriers are also scattered by the pore-edge electrical field that is formed as a result of charges trapped by pore-edges and is associated with a depletion region.⁵⁵ In detailed analysis, the scattering rate of this potential field can be calculated⁵⁶ and then added to l_E using the Matthiessen's Rule, with the unknown energy barrier height as a fitting parameter.⁶

FIG. 2. Lattice thermal conductivity per unit characteristic nanostructure size k_L/a for nanoporous Si. Comparison of calculations with all phonons (solid line) and only acoustic phonons (dashed line).

It should be noted that there exist numerous theoretical and experimental studies on phonon transport within Si films with periodically patterned nanopores.^{48–54,57–70} For a film with hexagonal packed pores,⁴⁹ $ZT \sim 0.4$ has been achieved at room temperature, in which measured k values (1.14 to 2.03 W/m·K) are two orders of magnitudes lower than that for the bulk Si (150 W/m·K). The observed k_L is often much lower than Eq. (1) predictions assuming diffusive phonon scattering on pore edges. This divergence is mainly attributed to phononic effects due to coherent interference of phonons reflected by periodic pore edges,⁵¹ and/or amorphous pore edges that introduce

non-propagating lattice-vibration modes.⁶³ For thin films with nanofabricated porous structures, the proposed ZT estimation can thus be treated as the lower bound of the real ZT value due to further k_L reduction by the above-mentioned two effects. For bulk materials, nanoporous structures can be formed by hot pressing nanoparticles without full compaction.⁷¹ Phononic effects are not anticipated in these random porous structures and Eq. (1) predictions can be more accurate. A comparably high ZT can also be achieved in nanowires with electron and phonon MFPs restricted by the nanowire diameter. These nanowires can be fabricated into devices⁷² or be joined as a bulk material⁷³ for TE applications.

To evaluate the additional contribution by optical phonons, k_L is evaluated with and without considering the optical branches (Fig. 2). At 300 K, 24% of k_L is contributed by the optical phonons under the SNS limit, in comparison to less than 10% in bulk Si.^{21,22} In heavily doped TE samples, however, the optical phonon contribution to k_L can be largely suppressed by impurity-phonon scattering that are more effective for low-group-velocity and high-frequency phonons. Instead of completely neglecting these optical branches, their contribution to k_L can also be estimated as the theoretical minimum for amorphous solids, in which the phonon MFPs become half of the phonon wavelength.^{74–76} In this work, ZT s are estimated with and without considering the optical phonon contribution to k_L , which can be viewed as the upper and lower bounds of the actual ZT s. An even higher ZT is anticipated in bulk materials with multi-length scale structures to suppress phonon transport across the whole phonon spectrum, while minimizing the negative impact on electron transport.^{2–4,77,78} In general, Eq. (3) can be used for fast-screening of novel materials and the obtained ZT can be improved by multi-length scale structures in a bulk material.

C. Estimation of the required nanostructure size for SNS limit

The SNS limit is approached when the phonon MFPs are largely restricted and k_L starts to scale down with the characteristic length a . For high-temperature applications, Umklapp scattering is the dominant phonon scattering mechanism and its relaxation time is given as⁷⁶

$$\tau_U(\omega) = \frac{(6\pi^2)^{1/3}}{2} \frac{\bar{M}v_g v_p^2}{k_B T V^{1/3} \gamma^2 \omega^2}, \quad (4)$$

where \bar{M} is the average atomic mass, V is volume per atom, γ is the Grüneisen parameter, and v_g and v_p are the phonon group and phase velocity, respectively. The bulk phonon MFP $l^{\text{Bulk}} = v_g \tau_U$ is further modified by the structure size a so that the MFP of the nanostructure is $l_{P,i}(\omega) =$

$[1/l_{P,i}^{\text{Bulk}}(\omega) + 1/a]^{-1}$. In Fig. 3(a) and (b) we plotted the calculated k_L for representative oxides as a function of the nanostructure size a . The parameters used in τ_U calculations are adopted from the supplementary material of Ref. 76. It can be observed that the SNS limit is approached for $a \sim 10$ nm at 300 K and ~ 2 nm at 1000 K. Although the latter may involve corrected phonon dispersion and electronic band structure of ultra-fine nanostructure, ZT values close to the SNS limit is anticipated at 10 nm structure sizes.

In most materials, the phonon MFPs distribute over a wide range, typically from a few nanometers to micrometers.^{79,80} To illustrate the phonon MFP distribution, in Fig. 3(c) we show the normalized accumulative k_L for ZnO at 300 K and 1000 K. The accumulative thermal conductivity is defined as⁸¹

$$k_{\text{accumu}}(l) = \int_0^l k_L(l') dl', \quad (5)$$

to show the contribution to the total k_L from phonons with different MFPs. At 300 K, phonons with MFPs larger than ~ 30 nm contribute 50% of the bulk ZnO k_L . Phonon MFPs decrease at elevated temperatures. At 1000 K, phonons with MFPs larger than 9 nm contribute 50% of the k_L . The averaged electron MFP of ZnO has been reported to be 21 nm in ZnO films at room temperature,⁸² and can be estimated to be ~ 5 nm at 1200 K since $\sigma \propto T^{-1}$.⁸³ For general oxides, such nanostructure sizes can be achieved in thin film by nanofabrication and potentially in bulk materials.

FIG. 3. Calculated lattice thermal conductivity at (a) 300 K and (b) 1000 K for SrO (squares) and ZnO (circles) as function of characteristic nanostructure size. (c) Normalized accumulative thermal conductivity of ZnO.

III. RESULTS AND DISCUSSION

Within the scope of this work, the focus is on novel oxides as high-temperature TE materials, which can recover high-quality waste heat from various resources such as industrial furnaces, airplane jet engines, and power plants. In addition to their high-temperature stability, all computed oxides possess a wide bandgap (> 2.1 eV) to prevent the detrimental bipolar conduction that is caused by minority charge carriers thermally excited at elevated temperatures.¹ These minority charge carriers cancel out S mediated by majority charge carriers (lower $S^2\sigma$) and simultaneously

FIG. 4. (Color online) Fermi-level (E_F) dependence of (a) k_E/a , (b) σ/a , (c) S , (d) $S^2\sigma/a$, and (e) ZT for representative oxides at 1250 K. All five plots assume $E_F = 0$ in the middle of the band gap. (f) Temperature-dependent ZT s of these oxides using the carrier concentration associated with E_F optimized at 1250 K.

increase k_E (and thus k), resulting in decreased ZT above a threshold temperature. In this aspect, a sufficiently large bandgap of oxides is crucial to maintaining a high ZT at high temperatures.

A. ZT of standard materials under SNS limit

Two n-type (wurtzite ZnO, SnO₂) and two p-type oxides (ZrOS, Ca₄P₂O) as wide-bandgap electrode materials are first investigated at 1250 K. With a high melting point $T_m > 2000$ K, these materials and their nanostructures can be thermally stable at ~ 1250 K during long-term operations, as shown in previous studies on ZnO.⁸⁴ The selection of electrode materials for TE applications is somewhat anticipated because all existing TE materials tend to have a high room-temperature σ ($\sim 1 \times 10^5$ S/m), as suggested by the database of existing TE materials.⁸⁵ For device fabrication, such electrode materials can also form superior electrical contacts to minimize Joule heating on junctions to avoid energy loss. At 1250 K, the computed k_E/a , σ/a , S , $S^2\sigma/a$, and ZT are plotted as functions of E_F in Figs. 4(a)–(e), respectively. As more conservative ZT estimation, both acoustic and optical branches are considered for k_L calculations. If effective p-type doping can be achieved, ZT_{1250K} around 1.4 can be obtained in Ca₄P₂O. In real samples, this ZT can be even higher due to the limited contribution of optical phonons.

The carrier concentration associated with the optimized E_F is further used to predict their temperature-dependent ZT s (Fig. 4(f)) across the whole temperature range, which monotonically increases with elevated temperatures for wide-bandgap materials. More accurate analysis should further consider the dopant activation at varied temperatures, in which the impurity energy level of the selected dopant and its possible impact on the electronic band structure can also be predicted by first principles.^{86,87} Although high ZT s are anticipated for p-type ZnO and SnO₂, only their n-type ZT s are considered here due to the long-term challenge in their p-type doping.^{88,89}

Under the SNS limit, analysis based on a single parabolic band suggests that a large effective mass will always benefit $S^2\sigma$ so that heavy holes are thus better than light electrons.¹⁶ In addition, a high effective mass also leads to a lower σ and thus reduced $k_E = L\sigma T$ to benefit the ZT , where

TABLE I. Thermoelectric properties calculated at 1250 K. ZnO and SnO₂ are n-doped and Fermi energy E_F are referenced from the conduction band bottom; Ca₄P₂O and ZrOS are p-doped and E_F are referred to the valence band top.

material	S	σ/a	$S^2\sigma/a$	k_L/a	k_E/a	$E_F - E_{\text{edge}}$	doping	ZT
	($\mu\text{V/K}$)	($\text{S m}^{-1} \text{nm}^{-1}$)	($\mu\text{W cm}^{-1} \text{K}^{-2} \text{nm}^{-1}$)	($\text{W m}^{-1} \text{K}^{-1} \text{nm}^{-1}$)		(meV)	(cm^{-3})	
ZnO	-162.3	6.015×10^3	1.585	1.832	0.146	70.9	-3.0×10^{19}	0.100
SnO ₂	-149.8	5.188×10^3	1.498	1.980	0.119	-34.0	-2.5×10^{19}	0.089
Ca ₄ P ₂ O	253.6	2.478×10^4	15.94	0.978	0.473	138	2.8×10^{20}	1.37
ZrOS	223.6	2.895×10^4	14.48	2.013	0.717	180	1.9×10^{20}	0.66

the Lorenz number L is roughly $2.4 \times 10^{-8} \text{W}\Omega\text{K}^{-2}$ for heavily doped samples.¹ The reduced k_E becomes more important to nanostructured materials with largely suppressed k_L . Among these four materials, the slightly higher $S^2\sigma/a$ of n-type Ca₄P₂O and ZrOS are due to additional electron valleys close to the conduction band edge, which function as extra “electron pockets” to increase σ for the same E_F . Such band degeneracy has been used to achieve a high power factor and thus ZT in PbTe_{1-x}Se_x and Mg₂Si_{1-x}Sn_x alloys.^{90,91} In nanoporous Ca₄P₂O and ZrOS, $S^2\sigma/a$ of n-type samples benefits from these additional electron valleys but the maximum ZT s of p-type samples are still higher due to their lower k_E (Fig. 4(a)).

Detailed information for optimized E_F and other properties are summarized in Table I. In general, maximized ZT is obtained at $|S|$ from 191 to 260 $\mu\text{V/K}$, which are higher than those to maximize $S^2\sigma$ (100–170 $\mu\text{V/K}$). The latter is comparable to the 130–187 $\mu\text{V/K}$ range suggested for optimum $S^2\sigma$ of conventional materials.⁹² Under the SNS limit, k_E becomes comparable to k_L so that the S optimization is an intermediate situation between two extreme cases, i.e. $k_E \gg k_L$ and $k_E \ll k_L$. The $S^2\sigma$ optimization applies to the ZT optimization under the condition $k_E \ll k_L$. As an opposite case, $k_E \gg k_L$ leads to $ZT \approx S^2\sigma T/k_E = S^2\sigma T/L\sigma T = S^2/L$ and a larger $|S|$ always benefits the ZT . In practice, the increased optimum $|S|$ under the SNS limit indicates a lower doping level that is less challenging in experiments.

With four atoms per primitive unit cell, wurtzite ZnO is predicted to reach $ZT_{1250\text{K}} = 0.10$ under the SNS limit. This value can be treated as the lower ZT bound because the nine optical branches may be largely overestimated for their k_L contribution, particularly the upper six optical branches with significantly higher frequencies than the rest phonon branches. When only three acoustic

FIG. 5. (Color online) (a) $S^2\sigma/a$ and $|S|$ for optimized ZT_{800K} of selected oxides. (b) k_L/a and k_E/a for the same cases. (c) Temperature-dependent ZT s of p-type CuAlO_2 and HfOS for both types using carrier concentration associated with the optimized E_F at 800 K.

FIG. 6. (Color online) Optimized ZT_{800K} as a function of (a) band gap E_g and (b) number n of atoms per primitive cell. (c) k_L dependence on n (circles for all branches, squares for acoustic branches only, lines as power-law fits).

branches are considered for k_L , ZT_{1250K} increases to 0.31 as the upper ZT bound. The actual ZT value should be within the 0.10–0.31 range but is still lower than $ZT_{1250K} \approx 0.65$ reported for Al-doped ZnO with isolated pores (100–200 nm in diameter),⁷¹ which further benefits from the electronic band structure variation of doped ZnO⁸⁷ and strong k_L reduction due to the alloy scattering of phonons. Depending on the material synthesis, nanoprecipitates often form within bulk ZnO to further reduce k_L but still maintain the PF.⁹³ In other theoretical studies, it has been pointed out that high ZT s of ZnO alloys depend on an unusual temperature dependence of the thermal conductivity.⁸³

B. ZT of general oxides under SNS limit

As more general cases, other oxides selected from the Inorganic Crystal Structure Database (ICSD) are optimized for their ZT s. Without the thermal stability information for some oxides, all ZT optimizations are thus carried out at 800 K that is generally safe for oxides. The obtained $S^2\sigma/a$, S , k_L/a , and k_E/a are shown in Figs. 5(a) and 5(b). As the major p-type electrode materials,⁹⁴ CuAlO_2 can achieve $ZT_{800K} > 1$ under the SNS limit and similarly high ZT s are also predicted for p- and n-type HfOS (Fig. 5(c)).

As general trends, the optimized ZT_{800K} values are plotted as a function of the band gap E_g (Fig. 6(a)) and atom number n within a primitive cell (Fig. 6(b)). Figure 6(a) shows that the optimized ZT s may still increase when $E_g \gg k_B T$, where T is operation temperature. In bulk materials, E_g of $6\text{--}10k_B T$ is suggested for best TE materials with indirect bandgap,^{95,96} while direct bandgap materials with special scattering mechanism of charge carriers may have $E_g > 10k_B T$ for optimum ZT .⁹⁷ These studies assume a bandgap-independent k_L but the actual ZT for a wide-bandgap material often decreases significantly due to increased k_L . This rule becomes

invalid with the dramatic k_L reduction by nanostructures and alloying atoms, as shown in the high- ZT nanostructured ZnO alloys^{71,93} and GaN alloys.⁹⁸ Secondly, ZT monotonically increases with n (Fig. 6(b)). As suggested earlier, $S^2\sigma$ benefits from larger n .¹⁶ For phonons, there are 3 acoustic and $3(n-1)$ optical branches within a material. The fraction of optical phonons is increased for larger n and their contribution to k_L is usually weak in heavily doped TE materials with strong point-defect scattering of optical phonons. By neglecting optical branch contribution, $k_L \sim n^{-2/3}$ was proposed for bulk materials by Slack.⁹⁹ As the lower and upper bounds of k_L , considering only acoustic branches leads to $k_L \sim n^{-1.3}$ at 800 K (dashed line in Fig. 6(c)), whereas considering all branches gives $k_L \sim n^{-0.4}$ (solid line). The $k_L \sim n^{-1.3}$ dependence is close to the $k_L \sim n^{-1.0}$ trend estimated for acoustic modes under strong boundary scattering.⁷⁶

IV. CONCLUSIONS

In summary, a first-principles ZT evaluation of novel materials under the SNS limit is proposed in this work and demonstrated in representative oxides. This enables broad search of next-generation TE materials with low materials cost and environment beneficial. Unrestricted to oxides, the 181,362 crystal structures within the ICSD can be re-evaluated for TE applications. The materials search can be further extended to those that do not exist in nature but can be thermodynamically stable based according to their first-principles-computed formation energy.^{17,18,100} A more general approach of non-existing material predictions can be found for batteries,^{101,102} which can be extended to TE materials in the future.

ACKNOWLEDGMENTS

Na Lu thanks the support from NSF grant CMMI-1351817. Hongbo Zhao thanks support from National Natural Science Foundation of China (Grant No. 11074077). Qing Hao acknowledges the support from U.S. Air Force Office of Scientific Research for the studies of nanoporous thermoelectric materials (award number FA9550-16-1-0025). An allocation of computer time from the UA Research Computing High Performance Computing (HPC) and High Throughput Computing (HTC) at the University of Arizona is gratefully acknowledged.

Appendix A: Electronic properties calculations

The expressions of S and σ are given by solving the Boltzmann Transport Equation:

$$\sigma = -e^2 \int \sigma(\varepsilon) \left(-\frac{\partial f}{\partial \varepsilon} \right) d\varepsilon, \quad (\text{A1})$$

$$S = -\frac{e}{\sigma T} \int \sigma(\varepsilon)(\varepsilon - E_F) \left(-\frac{\partial f}{\partial \varepsilon} \right) d\varepsilon, \quad (\text{A2})$$

where E_F is the Fermi level, $f = [1 + \exp(\frac{\varepsilon - E_F}{k_B T})]^{-1}$ is the Fermi-Dirac distribution function and k_B is the Boltzmann constant. The function $\sigma(\varepsilon)$ is related to the relaxation time $\tau_{i,\mathbf{k}}$ and group velocity $\mathbf{v}_{i,\mathbf{k}}$ for an electron state with band index i and momentum \mathbf{k} within the electronic band structure. Because MFPs are limited by the grain size a , we have $\tau_{i,\mathbf{k}} = a/|\mathbf{v}_{i,\mathbf{k}}|$ and

$$\sigma(\varepsilon) = \frac{1}{8\pi^3} \sum_i \int_{\text{1BZ}} \frac{a}{|\mathbf{v}_{i,\mathbf{k}}|} (\mathbf{v}_{i,\mathbf{k}} \cdot \hat{\varepsilon})^2 \delta(\varepsilon - \varepsilon_{i,\mathbf{k}}) d\mathbf{k}, \quad (\text{A3})$$

where $\hat{\varepsilon}$ is the unit vector of the transport direction and the integration is across the first Brillouin zone (BZ). In addition, the electronic thermal conductivity k_E is given as

$$k_E = \frac{1}{T} \int \sigma(\varepsilon)(\varepsilon - E_F)^2 \left(-\frac{\partial f}{\partial \varepsilon} \right) d\varepsilon - \frac{e^2}{\sigma T} \left[\int \sigma(\varepsilon)(\varepsilon - E_F) \left(-\frac{\partial f}{\partial \varepsilon} \right) d\varepsilon \right]^2. \quad (\text{A4})$$

As the effective values within an isotropic nanograined bulk material, above electrical properties will be averaged over x, y, and z directions for $\hat{\varepsilon}$.

Appendix B: Detailed charge carrier analysis

For the purpose of calibration of electronic properties of Si with the established calculation, we choose the Vining model⁴⁶ and adopt its original parameters. A general form of $\text{Si}_{1-x}\text{Ge}_x$ was considered by Vining.⁴⁶ For pure Si, the Ge fraction x is set as zero. A simple two-band analytical electronic energy dispersion is assumed. The effective mass for both electron and hole are set to $m^* = 1.40m_e$, where m_e is the mass of electron.

The electrical conductivity for each band is given as

$$\sigma_i = \frac{e^2 (2m^* k_B T)^{3/2}}{m^* \pi^2 \hbar^3} \int_0^\infty \left(-\frac{\partial f}{\partial z} \right) \tau(z) dz, \quad (\text{B1})$$

where z is reduced charge carrier energy $z = E/k_B T$, with temperature T and Boltzmann constant k_B , $f = [1 + \exp(z - \eta)]^{-1}$ is Fermi-Dirac distribution function with reduced Fermi energy $\eta =$

$E_F/k_B T$. The subscript i can be either e indicating conduction band, or h for valence band. The total electrical conductivity is simply $\sigma = \sigma_e + \sigma_h$. The energy dependent charge carrier relaxation time $\tau(z)$ is discussed at the end of this Appendix.

The Seebeck coefficient for each band is given as

$$S_i = \mp \frac{k_B}{e} \frac{\int_0^\infty \left(-\frac{\partial f}{\partial z}\right) \tau(z) (z - \eta) z^{3/2} dz}{\int_0^\infty \left(-\frac{\partial f}{\partial z}\right) \tau(z) z^{3/2} dz}, \quad (\text{B2})$$

with ‘-’ for conduction band and ‘+’ for valence band. The overall Seebeck coefficient is obtained by weighting each band’s contribution by its normalized electrical conductivity

$$S = \frac{S_e \sigma_e + S_h \sigma_h}{\sigma_e + \sigma_h}. \quad (\text{B3})$$

The electrical thermal conductivity k_E is calculated using Wiedemann-Franz law by $k_E = L_0 \sigma T$, where the Lorenz number L_0 is the sum of three terms: the contribution from conduction band L_e , from valence band L_h , and bipolar contribution L_b . The contribution from each band is given as

$$L_i = \left(\frac{k_B}{e}\right)^2 \left[\frac{\int_0^\infty \left(-\frac{\partial f}{\partial z}\right) \tau(z) z^{7/2} dz}{\int_0^\infty \left(-\frac{\partial f}{\partial z}\right) \tau(z) z^{3/2} dz} - \left(\frac{\int_0^\infty \left(-\frac{\partial f}{\partial z}\right) \tau(z) z^{5/2} dz}{\int_0^\infty \left(-\frac{\partial f}{\partial z}\right) \tau(z) z^{3/2} dz} \right)^2 \right]. \quad (\text{B4})$$

The bipolar Lorenz number is given as

$$L_b = \frac{\sigma_e \sigma_h}{\sigma^2} (S_e - S_h)^2. \quad (\text{B5})$$

For our nanograined Si, we consider three charge carrier scattering mechanism, so that according to Matthiessen’s rule we have

$$\tau^{-1}(E) = \tau_{AC}^{-1}(E) + \tau_I^{-1}(E) + \tau_{NG}^{-1}(E), \quad (\text{B6})$$

where E is energy of charge carriers, τ_{AC} , τ_I , and τ_{NG} are relaxation time of scattering with intravalley acoustic phonon, ionized impurity, and nanograins, respectively. The last scattering is what differs from the Vining model.⁴⁶

Scattering with acoustic phonon is described with deformation potentials. Following Vining, deformation potential for both electrons and holes are identical as $E_d = 2.94$ eV.⁴⁶ We then have

$$\tau_{AC}^{-1}(E) = \frac{\pi E_d^2 k_B T}{\rho v_s^2 \hbar} D(E) \left(1 - \frac{8 E (E_g + E)}{3 (E_g + 2E)^2} \right), \quad (\text{B7})$$

where ρ is density, v_s is sound velocity, and electronic density of states is $D(E) = \frac{(2m^*)^{3/2}}{2\pi^2\hbar^3}\sqrt{E}$.

For scattering with ionized impurity, we use dielectric constant $\epsilon = 27.4$ (Ref. 46). The screening length r_s of Coulomb interaction is given as

$$r_s^{-2} = \frac{2^{5/2}e^2m^*\sqrt{k_B T}}{\pi\hbar^3\epsilon} \int_0^\infty \left(-\frac{\partial f}{\partial z}\right)z^{1/2}dz,$$

and relaxation time is given as

$$\tau_I^{-1}(E) = \frac{\pi(4\pi e^2/\epsilon)}{8\hbar k^4} D(E) \left(\ln(1 + \xi) - \frac{\xi}{1 + \xi} \right) N_D, \quad (\text{B8})$$

where N_D is number density of ionized impurity, and $\xi = (2kr_s)^2$.

Finally, scattering with nanograins can be calculated using the size of nanograin a and the parabolic band

$$\tau_{NG}^{-1}(E) = \frac{v}{a} = \frac{\sqrt{2E/m^*}}{a}. \quad (\text{B9})$$

Appendix C: Detailed phonon analysis

To simplify calculation, isotropic phonon dispersion is assumed here and the phonon dispersion along the (001) direction for bulk silicon¹⁰³ is employed. Only acoustic phonons are considered here without an explicit expression of energy-dependent optical phonon MFPs.

The phonon MFP $l_{P,i}(\omega)$ is modified from the bulk $l_{P,i}^{\text{Bulk}}(\omega)$ as $1/l_{P,i}(\omega) = 1/a + 1/l_{P,i}^{\text{Bulk}}(\omega)$. For $l_{P,i}^{\text{Bulk}}(\omega)$ computations, the bulk phonon lifetime, $\tau_{P,i}^{\text{Bulk}}(\omega) = l_{P,i}^{\text{Bulk}}(\omega)/v_i^P(\omega)$, is given by the Matthiessen's rule:

$$1/\tau_{P,i}^{\text{Bulk}}(\omega) = \tau_I^{-1}(\omega) + \tau_{N,i}^{-1}(\omega) + \tau_{U,i}^{-1}(\omega) + \tau_E^{-1}(\omega).$$

Here $\tau_I(\omega)$, $\tau_{N,i}(\omega)$, $\tau_{U,i}(\omega)$, and $\tau_E(\omega)$ are the phonon lifetime associated with impurity scattering, normal (N) process, Umklapp (U) process, and electron scattering, respectively.

Based on first-principles calculations on bulk Si, the relaxation times of the momentum-conserved N process and momentum-non-conserved U process are calculated as in Refs. 22 and 104,

$$\tau_{N,i}^{-1} = A_{N,i}(\hbar\omega)^2 T [1 - \exp(-3T/\Theta_D)], \quad (\text{C1})$$

$$\tau_{U,i}^{-1} = A_{U,i}(\hbar\omega)^4 T [1 - \exp(-3T/\Theta_D)], \quad (\text{C2})$$

TABLE CI. Parameters used for phonon-phonon scattering models of bulk Si. In the given relaxation time expressions, $\hbar\omega$ should be converted into meV to be consistent with the units of following $A_{N/U}$ values for LA and TA branches.

$A_{N,TA}$	$A_{N,LA}$	$A_{U,TA}$	$A_{U,LA}$	Θ_D
(meV ⁻² K ⁻¹ s ⁻¹)		(meV ⁻⁴ K ⁻¹ s ⁻¹)		(K)
147280	163921	1170	507	645

in which T is the absolute temperature, \hbar is the Planck constant divided by 2π , Θ_D is the Debye temperature, $A_{N/U,i}$ is material-dependent coefficient further modified for isotropic phonon dispersion of Si (Table CI).⁴⁵

For natural Si with isotopes, the impurity-phonon scattering $\tau_i(\omega)$ is given as in Ref. 105,

$$\tau_i^{-1}(\omega) = \frac{\pi}{6} V_0 g \omega^2 D(\omega), \quad (\text{C3})$$

where V_0 is the averaged volume per atom (2.0×10^{-29} m³ for Si), g is the mass variance determined by the composition, $D(\omega)$ is the phonon density of states at ω . Here $g = \sum_j f_j (1 - m_j/\bar{m})^2$, with m_j as the atomic mass for the j -th isotope, f_j the molar percentage of individual isotope atoms, and $\bar{m} = \sum_j f_j m_j$ the averaged atomic mass. In heavily doped n-type silicon ($n > 1.0 \times 10^{18}$ cm⁻³), shallow impurity levels within the band gap start to merge with the conduction band so that the dopants are always completely ionized.¹⁰⁶ For a carrier concentration of 2×10^{20} cm⁻³, there is 0.4 mol% phosphorus atoms in Si and g is estimated to be 2.41×10^{-4} , which is slightly higher than $g = 2.01 \times 10^{-4}$ for natural Si.¹⁰⁷

For heavily doped TE materials, the electron scattering of phonons plays an important role in its k_L reduction and $\tau_E(\omega)$ is expressed as

$$\tau_E^{-1}(\omega) = \frac{E_d^2 m^{*3} v_g}{4\pi \hbar^4 d} \frac{k_B T}{\frac{1}{2} m^* v_g^2} \left[\frac{\hbar\omega}{k_B T} - \ln \frac{1 + \exp\left(\frac{\frac{1}{2} m^* v_g^2 - E_F}{k_B T} + \frac{\hbar^2 \omega^2}{8 m^* v_g^2 k_B T} + \frac{\hbar\omega}{2 k_B T}\right)}{1 + \exp\left(\frac{\frac{1}{2} m^* v_g^2 - E_F}{k_B T} + \frac{\hbar^2 \omega^2}{8 m^* v_g^2 k_B T} - \frac{\hbar\omega}{2 k_B T}\right)} \right], \quad (\text{C4})$$

in which k_B is the Boltzmann constant, $E_d = 2.938$ eV is the acoustic deformation potential, $m^* = 1.40 m_e$ is the density-of-states effective mass, m_e is the free electron mass, $d = 2327$ kg/m³ is the density, $v_g = 5880$ m/s is the averaged phonon group velocity,⁴⁶ and E_F (0.082 eV at 300 K,

0.0036 eV at 1000 K) is the computed Fermi energy referred to the conduction band edge.

* qinghao@email.arizona.edu

† zhaohb@scnu.edu.cn

¹ H. J. Goldsmid, *Thermoelectric Refrigeration* (Plenum Press, New York, 1964).

² A. J. Minnich, M. S. Dresselhaus, Z. F. Ren, and G. Chen, *Energy Environ. Sci.* **2**, 466 (2009).

³ B. Poudel, Q. Hao, Y. Ma, Y. Lan, A. Minnich, B. Yu, X. Yan, D. Wang, A. Muto, D. Vashaee, X. Chen, J. Liu, M. S. Dresselhaus, G. Chen, and Z. Ren, *Science* **320**, 634 (2008).

⁴ K. Biswas, J. He, I. D. Blum, C.-I. Wu, T. P. Hogan, D. N. Seidman, V. P. Dravid, and M. G. Kanatzidis, *Nature* **489**, 414 (2012).

⁵ S. K. Bux, R. G. Blair, P. K. Gogna, H. Lee, G. Chen, M. S. Dresselhaus, R. B. Kaner, and J.-P. Fleurial, *Adv. Func. Mater.* **19**, 2445 (2009).

⁶ Q. Hao, G. Zhu, G. Joshi, X. Wang, A. Minnich, Z. Ren, and G. Chen, *Appl. Phys. Lett.* **97**, 063109 (2010).

⁷ X. W. Wang, H. Lee, Y. C. Lan, G. H. Zhu, G. Joshi, D. Z. Wang, J. Yang, A. J. Muto, M. Y. Tang, J. Klatsky, S. Song, M. S. Dresselhaus, G. Chen, and Z. F. Ren, *Appl. Phys. Lett.* **93**, 193121 (2008).

⁸ Y. Ma, Q. Hao, B. Poudel, Y. Lan, B. Yu, D. Wang, G. Chen, and Z. Ren, *Nano Lett.* **8**, 2580 (2008).

⁹ G. Joshi, H. Lee, Y. Lan, X. Wang, G. Zhu, D. Wang, R. W. Gould, D. C. Cuff, M. Y. Tang, M. S. Dresselhaus, G. Chen, and Z. Ren, *Nano Lett.* **8**, 4670 (2008).

¹⁰ G. H. Zhu, H. Lee, Y. C. Lan, X. W. Wang, G. Joshi, D. Z. Wang, J. Yang, D. Vashaee, H. Guilbert, A. Pillitteri, M. S. Dresselhaus, G. Chen, and Z. F. Ren, *Phys. Rev. Lett.* **102**, 196803 (2009).

¹¹ S. M. Kauzlarich, S. R. Brown, and G. J. Snyder, *Dalton Trans.*, 2099 (2007).

¹² A. F. May, J.-P. Fleurial, and G. J. Snyder, *Phys. Rev. B* **78**, 125205 (2008).

¹³ L. R. Danielson, M. N. Alexander, C. Vining, R. A. Lockwood, and C. Wood, in *Proceedings of the Seventh International Conference on Thermoelectric Energy Conversion* (University of Texas at Arlington, 1988) pp. 71–75.

¹⁴ C. Vining, C. Wood, J. Parker, A. Zoltan, L. Danielson, and M. Alexander, in *Proceedings of the Seventh International Conference on Thermoelectric Energy Conversion* (University of Texas at Arlington, 1988) pp. 9–13.

¹⁵ S. Curtarolo, G. L. W. Hart, M. B. Nardelli, N. Mingo, S. Sanvito, and O. Levy, *Nat. Mater.* **12**, 191

- (2013).
- ¹⁶ S. Wang, Z. Wang, W. Setyawan, N. Mingo, and S. Curtarolo, *Phys. Rev. X* **1**, 021012 (2011).
 - ¹⁷ I. Opahle, G. K. H. Madsen, and R. Drautz, *Phys. Chem. Chem. Phys.* **14**, 16197 (2012).
 - ¹⁸ I. Opahle, A. Parma, E. J. McEniry, R. Drautz, and G. K. H. Madsen, *New J. Phys.* **15**, 105010 (2013).
 - ¹⁹ G. K. H. Madsen, *J. Am. Chem. Soc.* **128**, 12140 (2006).
 - ²⁰ G. K. H. Madsen and D. J. Singh, *Comput. Phys. Commun.* **175**, 67 (2006).
 - ²¹ K. Esfarjani, G. Chen, and H. T. Stokes, *Phys. Rev. B* **84**, 085204 (2011).
 - ²² A. Ward and D. A. Broido, *Phys. Rev. B* **81**, 085205 (2010).
 - ²³ D. A. Broido, M. Malorny, G. Birner, N. Mingo, and D. A. Stewart, *Appl. Phys. Lett.* **91**, 231922 (2007).
 - ²⁴ L. Lindsay, D. A. Broido, and T. L. Reinecke, *Phys. Rev. Lett.* **109**, 095901 (2012).
 - ²⁵ L. Lindsay, D. A. Broido, and T. L. Reinecke, *Phys. Rev. Lett.* **111**, 025901 (2013).
 - ²⁶ Z. Tian, J. Garg, K. Esfarjani, T. Shiga, J. Shiomi, and G. Chen, *Phys. Rev. B* **85**, 184303 (2012).
 - ²⁷ M. Lundstrom, *Fundamentals of Carrier Transport*, 2nd ed. (Cambridge University Press, 2000).
 - ²⁸ O. D. Restrepo, K. Varga, and S. T. Pantelides, *Appl. Phys. Lett.* **94**, 212103 (2009).
 - ²⁹ F. Murphy-Armando and S. Fahy, *Phys. Rev. B* **78**, 035202 (2008).
 - ³⁰ J. Sjakste, N. Vast, and V. Tyuterev, *Phys. Rev. Lett.* **99**, 236405 (2007).
 - ³¹ Z. Wang, S. Wang, S. Obukhov, N. Vast, J. Sjakste, V. Tyuterev, and N. Mingo, *Phys. Rev. B* **83**, 205208 (2011).
 - ³² P. Poopanya, *Phys. Lett. A* **379**, 853 (2015).
 - ³³ L. Xi, Y. B. Zhang, X. Y. Shi, J. Yang, X. Shi, L. D. Chen, W. Zhang, J. Yang, and D. J. Singh, *Phys. Rev. B* **86**, 155201 (2012).
 - ³⁴ A. N. Qiu, L. T. Zhang, and J. S. Wu, *Phys. Rev. B* **81**, 035203 (2010).
 - ³⁵ C. Bera, M. Soulier, C. Navone, G. Roux, J. Simon, S. Volz, and N. Mingo, *J. Appl. Phys.* **108**, 124306 (2010).
 - ³⁶ V. Jean, S. Fumeron, K. Termentzidis, S. Tutashkonko, and D. Lacroix, *J. Appl. Phys.* **115**, 024304 (2014).
 - ³⁷ A. Minnich and G. Chen, *Appl. Phys. Lett.* **91**, 073105 (2007).
 - ³⁸ G. D. Mahan and J. O. Sofo, *Proc. Natl. Acad. Sci. USA* **93**, 7436 (1996).
 - ³⁹ A. Eucken, *Ceram. Abs.* **11**, 576 (1932).
 - ⁴⁰ A. Eucken, *Ceram. Abs.* **12**, 231 (1933).

- ⁴¹ G. Kresse and J. Furthmüller, Phys. Rev. B **54**, 11169 (1996).
- ⁴² G. Kresse and D. Joubert, Phys. Rev. B **59**, 1758 (1999).
- ⁴³ J. P. Perdew, K. Burke, and M. Ernzerhof, Phys. Rev. Lett. **77**, 3865 (1996).
- ⁴⁴ A. Togo, F. Oba, and I. Tanaka, Phys. Rev. B **78**, 134106 (2008).
- ⁴⁵ Q. Hao, J. Appl. Phys. **116**, 034305 (2014).
- ⁴⁶ C. B. Vining, J. Appl. Phys. **69**, 331 (1991).
- ⁴⁷ J. Dura, S. Martinie, D. Munteanu, F. Triozon, S. Barraud, Y.-M. Niquet, and J.-L. Aufran, in *Electrostatics* (InTech, 2012) pp. 113–136.
- ⁴⁸ J.-K. Yu, S. Mitrovic, D. Tham, J. Varghese, and J. R. Heath, Nat. Nanotechnol. **5**, 718 (2010).
- ⁴⁹ J. Tang, H.-T. Wang, D. H. Lee, M. Fardy, Z. Huo, T. P. Russell, and P. Yang, Nano Lett. **10**, 4279 (2010).
- ⁵⁰ A. M. Marconnet, T. Kodama, M. Asheghi, and K. E. Goodson, Nanoscale Microscale Thermophys. Eng. **16**, 199 (2012).
- ⁵¹ Q. Hao, D. Xu, and H. Zhao, in *MRS Proceedings*, Vol. 1779 (2015) p. 2732.
- ⁵² D. Song and G. Chen, Appl. Phys. Lett. **84**, 687 (2004).
- ⁵³ P. E. Hopkins, C. M. Reinke, M. F. Su, R. H. Olsson, E. A. Shaner, Z. C. Leseman, J. R. Serrano, L. M. Phinney, and I. El-Kady, Nano Lett. **11**, 107 (2011).
- ⁵⁴ B. Kim, J. Nguyen, P. J. Clews, C. M. Reinke, D. Goettler, Z. C. Leseman, I. El-Kady, and R. H. Olsson, in *2012 IEEE 25th International Conference on Micro Electro Mechanical Systems (MEMS)* (2012) pp. 176–179.
- ⁵⁵ C. R. M. Grovenor, J. Phys. C: Solid State Phys. **18**, 4079 (1985).
- ⁵⁶ A. J. Minnich, H. Lee, X. W. Wang, G. Joshi, M. S. Dresselhaus, Z. F. Ren, G. Chen, and D. Vashaee, Phys. Rev. B **80**, 155327 (2009).
- ⁵⁷ J.-H. Lee, G. A. Galli, and J. C. Grossman, Nano Lett. **8**, 3750 (2008).
- ⁵⁸ E. Dechaumphai and R. Chen, J. Appl. Phys. **111**, 073508 (2012).
- ⁵⁹ P. Hyldgaard and G. D. Mahan, Phys. Rev. B **56**, 10754 (1997).
- ⁶⁰ M. V. Simkin and G. D. Mahan, Phys. Rev. Lett. **84**, 927 (2000).
- ⁶¹ S.-i. Tamura, Y. Tanaka, and H. J. Maris, Phys. Rev. B **60**, 2627 (1999).
- ⁶² M. Maldovan, Phys. Rev. Lett. **110**, 025902 (2013).
- ⁶³ Y. He, D. Donadio, J.-H. Lee, J. C. Grossman, and G. Galli, ACS Nano **5**, 1839 (2011).
- ⁶⁴ Y. He and G. Galli, Phys. Rev. Lett. **108**, 215901 (2012).

- ⁶⁵ J. Lee, J. Lim, and P. Yang, *Nano Lett.* **15**, 3273 (2015).
- ⁶⁶ A. Jain, Y.-J. Yu, and A. J. H. McGaughey, *Phys. Rev. B* **87**, 195301 (2013).
- ⁶⁷ N. K. Ravichandran and A. J. Minnich, *Phys. Rev. B* **89**, 205432 (2014).
- ⁶⁸ G. Romano and J. C. Grossman, *Appl. Phys. Lett.* **105**, 033116 (2014).
- ⁶⁹ G. Romano, A. D. Carlo, and J. C. Grossman, *J. Comput. Electron.* **11**, 8 (2012).
- ⁷⁰ J.-H. Lee, J. C. Grossman, J. Reed, and G. Galli, *Appl. Phys. Lett.* **91**, 223110 (2007).
- ⁷¹ M. Ohtaki and R. Hayashi, in *Proceedings ICT '06. 25th International Conference on Thermoelectrics* (Vienna, Austria, 2006) pp. 276–279.
- ⁷² G. Pennelli, *Beilstein J. Nanotechnol.* **5**, 1268 (2014).
- ⁷³ Y. Kang and S. Vaddiraju, *Chem. Mater.* **26**, 2814 (2014).
- ⁷⁴ A. Einstein, *Ann. Phys. (Berlin)* **35**, 679 (1911).
- ⁷⁵ D. G. Cahill, S. K. Watson, and R. O. Pohl, *Phys. Rev. B* **46**, 6131 (1992).
- ⁷⁶ E. S. Toberer, A. Zevalkink, and G. J. Snyder, *J. Mater. Chem.* **21**, 15843 (2011).
- ⁷⁷ L.-D. Zhao, V. P. Dravid, and M. G. Kanatzidis, *Energy Environ. Sci.* **7**, 251 (2013).
- ⁷⁸ J.-L. Lan, Y. Liu, Y.-H. Lin, C.-W. Nan, and X. Yang, *Sci. Rep.* **5**, 7783 (2015).
- ⁷⁹ T. Feng and X. Ruan, *J. Nanomater.* **2014**, 206370 (2014).
- ⁸⁰ K. T. Regner, J. P. Freedman, and J. A. Malen, *Nanoscale Microscale Thermophys. Eng.* **19**, 183 (2015).
- ⁸¹ C. Dames and G. Chen, in *Thermoelectrics Handbook: Macro to Nano* (CRC Press, Boca Raton, 2006) chap. 42.
- ⁸² J. B. Baxter and C. A. Schmuttenmaer, *J. Phys. Chem. B* **110**, 25229 (2006).
- ⁸³ K. P. Ong, D. J. Singh, and P. Wu, *Phys. Rev. B* **83**, 115110 (2011).
- ⁸⁴ M. Ohtaki, K. Araki, and K. Yamamoto, *J. Electron. Mater.* **38**, 1234 (2009).
- ⁸⁵ M. W. Gaultois, T. D. Sparks, C. K. H. Borg, R. Seshadri, W. D. Bonificio, and D. R. Clarke, *Chem. Mater.* **25**, 2911 (2013).
- ⁸⁶ Z. S. Popovic, S. Satpathy, and W. C. Mitchel, *Phys. Rev. B* **70**, 161308 (2004).
- ⁸⁷ S. Jantrasee, S. Pinitsoontorn, and P. Moontragoon, *J. Electron. Mater.* **43**, 1689 (2014).
- ⁸⁸ D. O. Scanlon and G. W. Watson, *J. Mater. Chem.* **22**, 25236 (2012).
- ⁸⁹ G. Brauer, J. Kuriplach, C. C. Ling, and A. B. Djurišić, *J. Phys.: Conf. Ser.* **265**, 012002 (2011).
- ⁹⁰ Y. Pei, X. Shi, A. LaLonde, H. Wang, L. Chen, and G. J. Snyder, *Nature* **473**, 66 (2011).
- ⁹¹ W. Liu, X. Tan, K. Yin, H. Liu, X. Tang, J. Shi, Q. Zhang, and C. Uher, *Phys. Rev. Lett.* **108**, 166601

- (2012).
- ⁹² P. Pichanusakorn and P. R. Bandaru, *Appl. Phys. Lett.* **94**, 223108 (2009).
- ⁹³ P. Jood, R. J. Mehta, Y. Zhang, G. Peleckis, X. Wang, R. W. Siegel, T. Borca-Tasciuc, S. X. Dou, and G. Ramanath, *Nano Lett.* **11**, 4337 (2011).
- ⁹⁴ H. Kawazoe, M. Yasukawa, H. Hyodo, M. Kurita, H. Yanagi, and H. Hosono, *Nature* **389**, 939 (1997).
- ⁹⁵ G. D. Mahan, *J. Appl. Phys.* **65**, 1578 (1989).
- ⁹⁶ R. P. Chasmar and R. Stratton, *J. Electron. Control* **7**, 52 (1959).
- ⁹⁷ J. O. Sofo and G. D. Mahan, *Phys. Rev. B* **49**, 4565 (1994).
- ⁹⁸ N. Lu and I. Ferguson, *Semicond. Sci. Technol.* **28**, 074023 (2013).
- ⁹⁹ G. A. Slack, in *Solid State Physics*, Vol. 34, edited by H. Ehrenreich, F. Seitz, and D. Turnbull (Academic Press, New York, 1979) pp. 1–71.
- ¹⁰⁰ G. Hautier, A. Miglio, G. Ceder, G.-M. Rignanese, and X. Gonze, *Nat. Commun.* **4**, 2292 (2013).
- ¹⁰¹ L. Yang and G. Ceder, *Phys. Rev. B* **88**, 224107 (2013).
- ¹⁰² G. Hautier, C. Fischer, V. Ehlacher, A. Jain, and G. Ceder, *Inorg. Chem.* **50**, 656 (2010).
- ¹⁰³ G. Nilsson and G. Nelin, *Phys. Rev. B* **6**, 3777 (1972).
- ¹⁰⁴ A. Ward, *First Principles of the Lattice Thermal Conductivity of Semiconductors*, Ph.D. thesis, Boston College, Chestnut Hill, MA (2009).
- ¹⁰⁵ S.-i. Tamura, *Phys. Rev. B* **27**, 858 (1983).
- ¹⁰⁶ V. I. Fistul and J. S. Blakemore, *Am. J. Phys.* **37**, 1291 (1969).
- ¹⁰⁷ A. V. Inyushkin, A. N. Taldenkov, A. M. Gibin, A. V. Gusev, and H.-J. Pohl, *Phys. Status Solidi C* **1**, 2995 (2004).

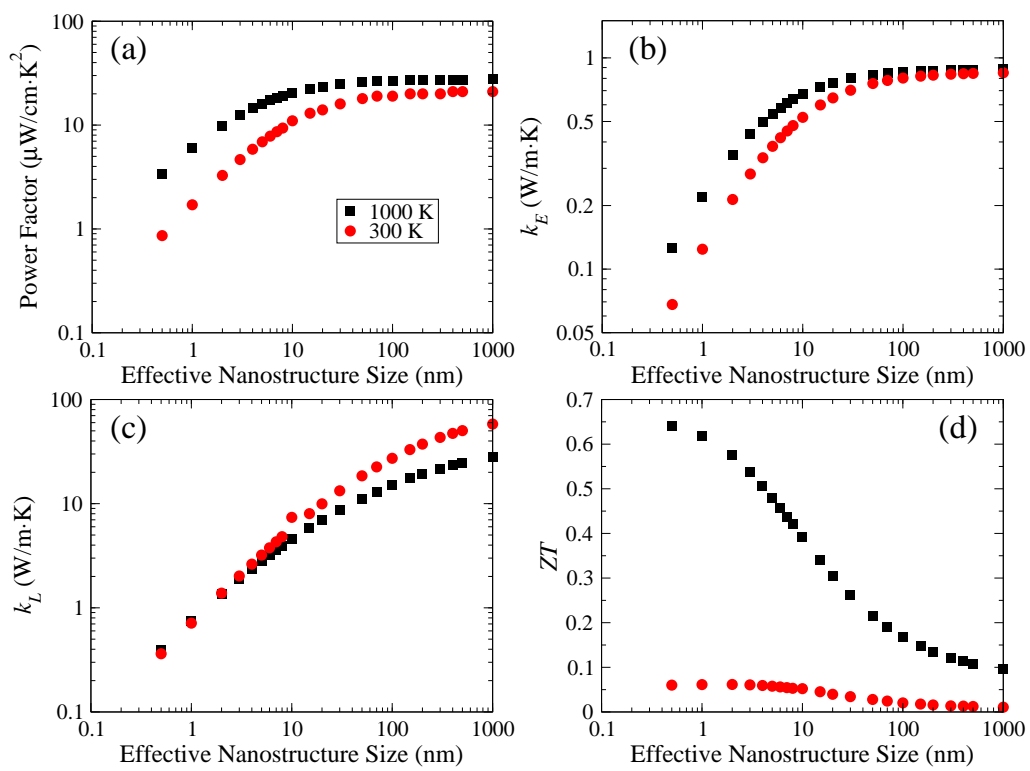


Figure 1

25Apr2016

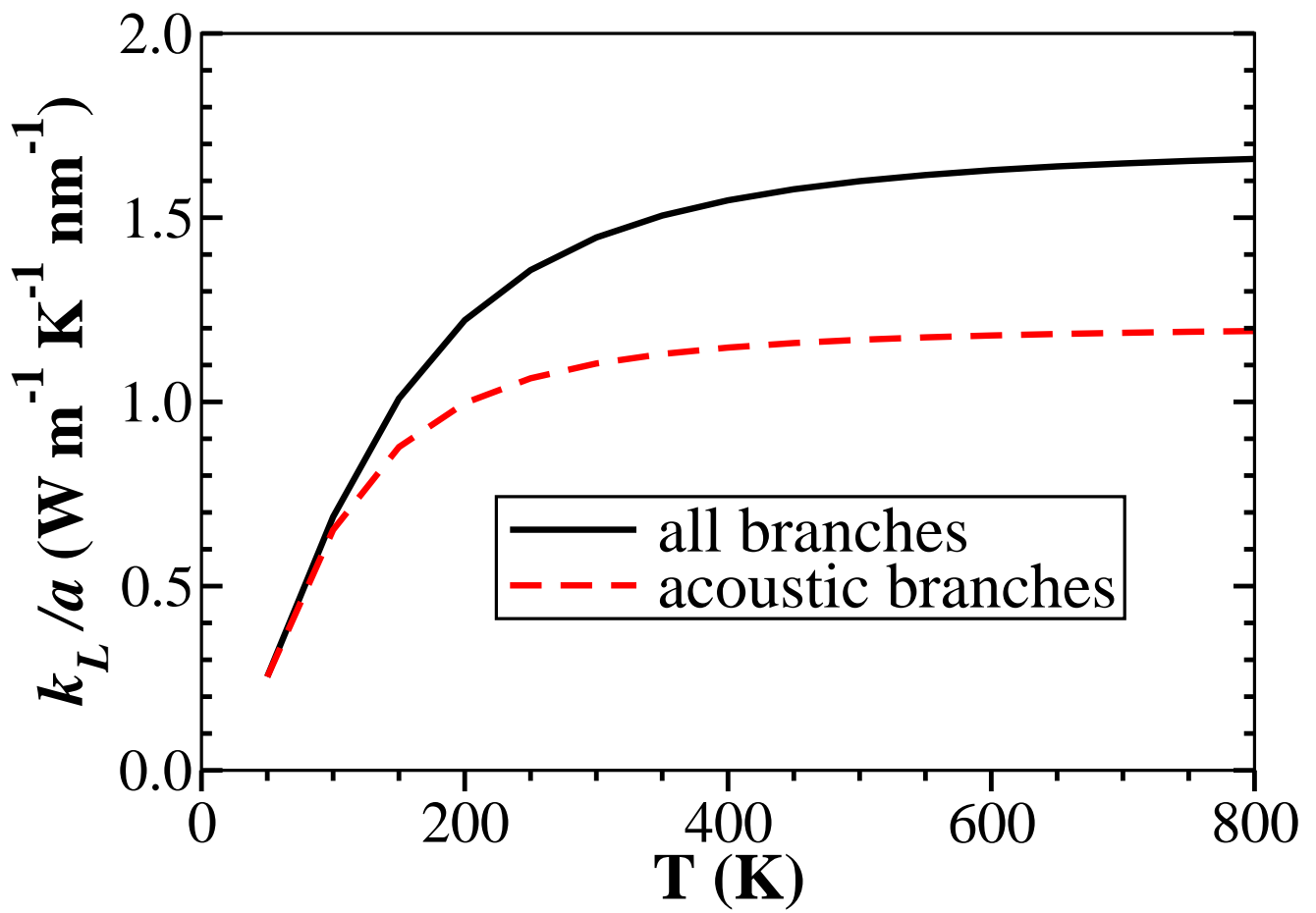


Figure 2

25Apr2016

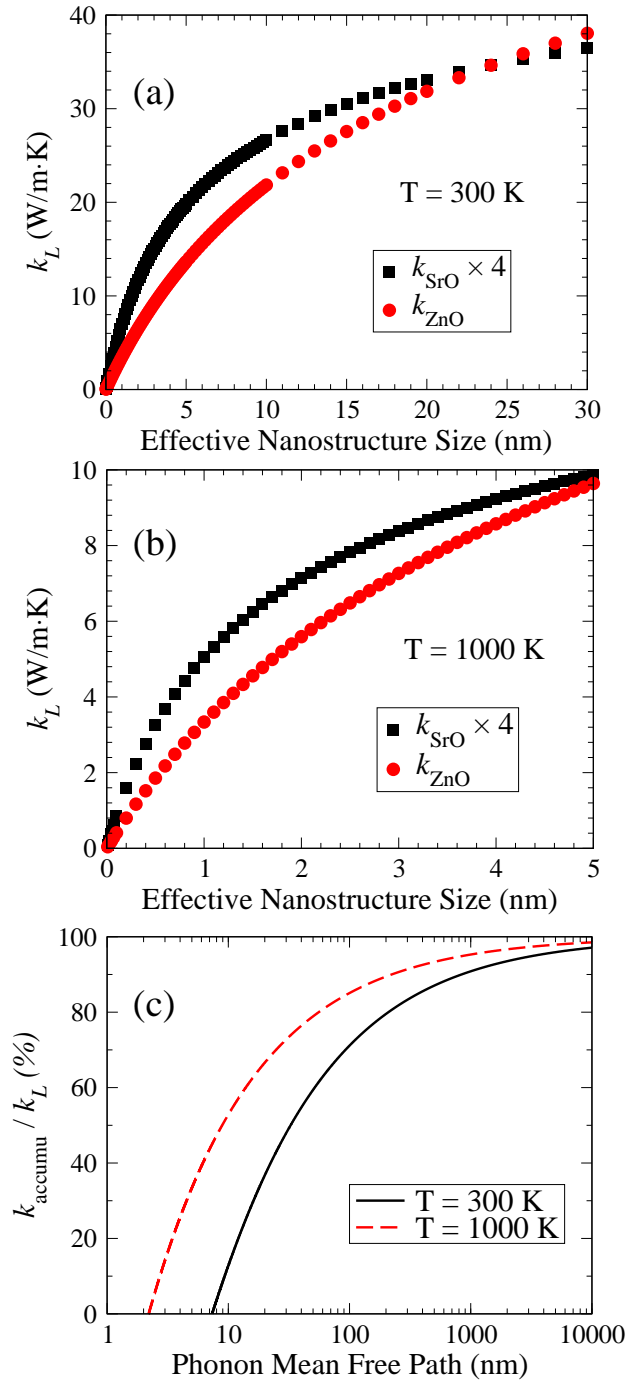


Figure 3

25Apr2016

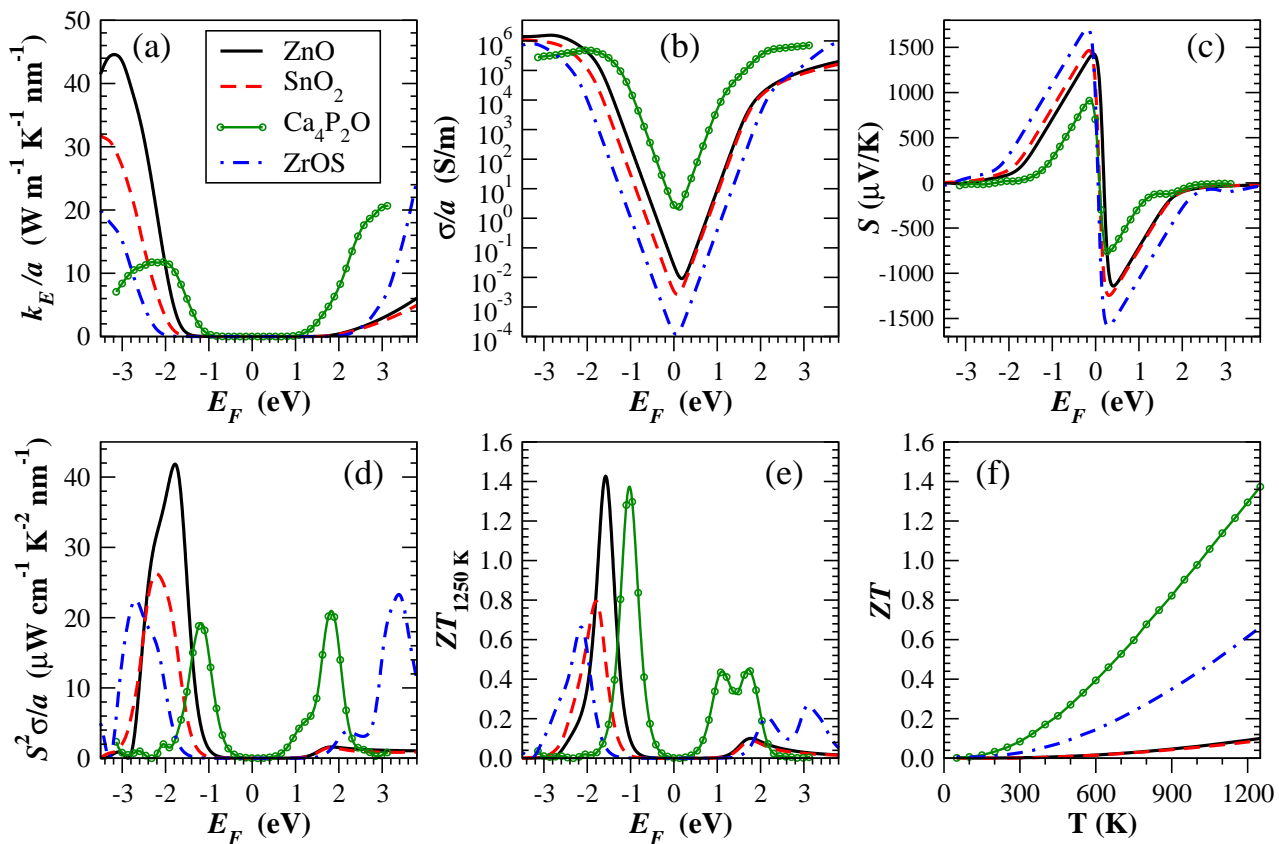


Figure 4

25Apr2016

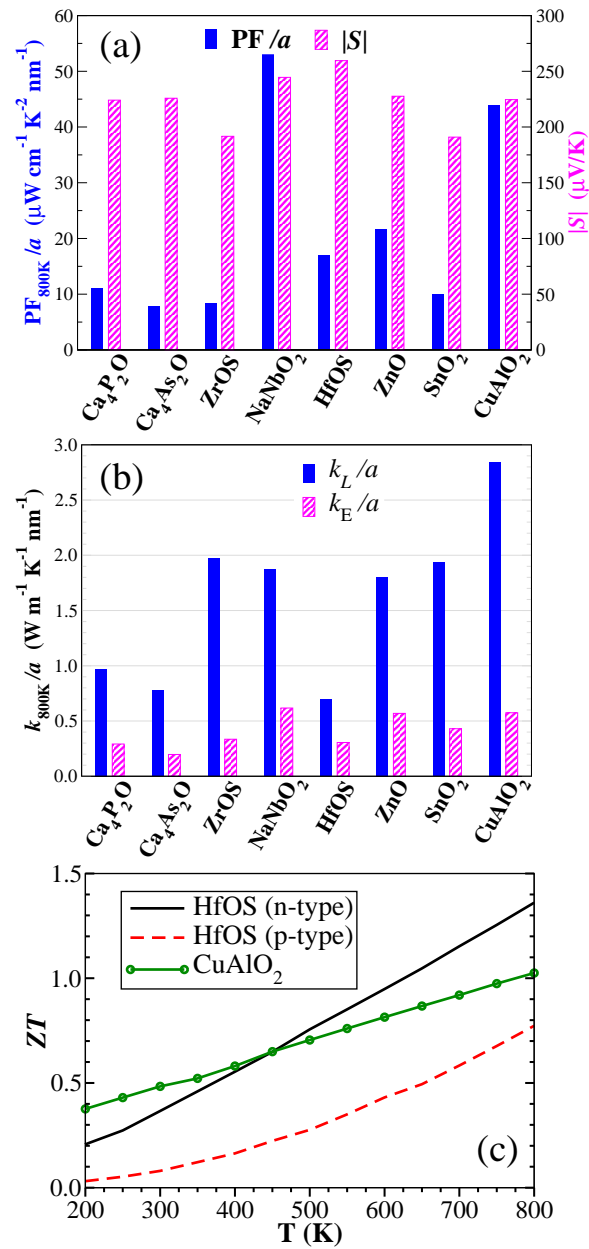


Figure 5

25Apr2016

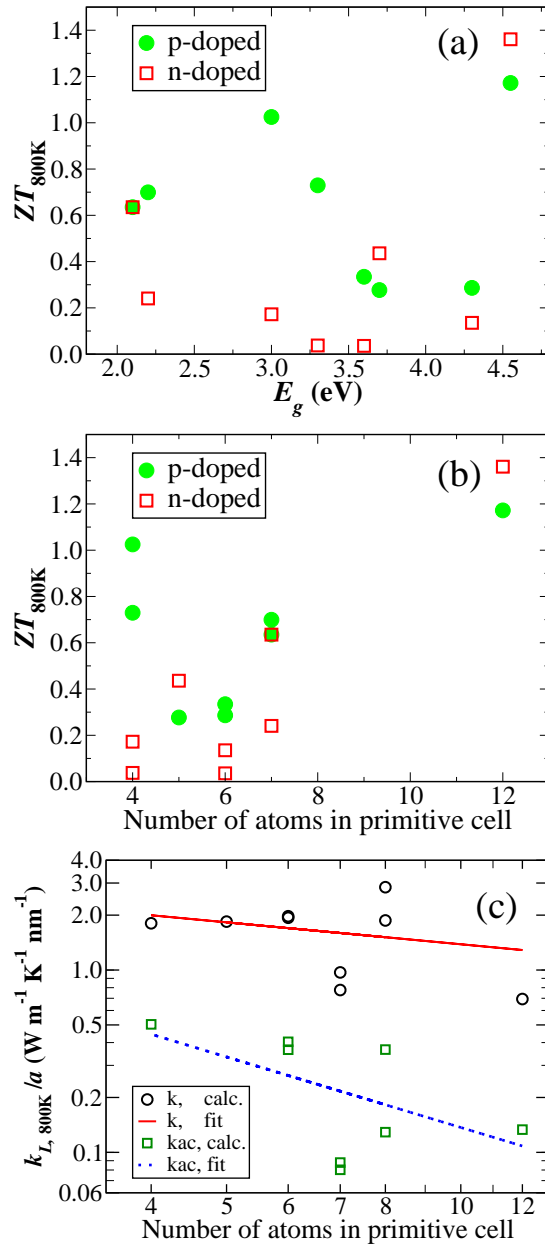


Figure 6

25Apr2016